

Article

The Perturbation of the Guadalupian Marine Environment Triggered by Early-Stage Eruption of the Emeishan Large Igneous Province: Rare Earth Element and Sr-Nd Isotope Evidence from Zunyi Manganese Deposit, South China

Hao Yan ^{1,2}, Daohui Pi ^{1,*}, Lingang Xu ³ and Kai Sun ³

¹ State Key Laboratory of Geological Processes and Mineral Resources, School of Earth Resources, China University of Geosciences, Wuhan 430074, China; 18630112659@163.com

² Institute of Earth Sciences, China University of Geosciences, Beijing 100083, China

³ School of Earth Sciences and Resources, China University of Geosciences, Beijing 100083, China; xulingang@cugb.edu.cn (L.X.); sk271884@163.com (K.S.)

* Correspondence: daohuipi@cug.edu.cn

Abstract: Pure marine chemical sediments are archives of geochemical proxies for the composition of seawater and may provide information about the ancient hydrosphere–atmosphere system. The early stage of the Emeishan large igneous province (ELIP) was characterized by the subaqueous eruption of mafic igneous rocks around the *J. altudaensis* zone of the Capitanian Stage that has been proposed to have contributed to the Guadalupian mass extinction. However, detailed mechanisms and the impact of the eruption on the Guadalupian marine environment have yet to be assessed. Here, to examine the Guadalupian marine environment, we studied major and trace element concentrations, particularly rare earth element and yttrium data, along with high-precision Sr-Nd isotope ratios, of three types of Mn ores (i.e., clastic, massive, and oolitic) and siliceous limestones from the Zunyi Mn deposit in South China formed following the early-stage eruption of the ELIP. Our results indicate that the clastic Mn ores contain notable detrital mafic aluminosilicates. In contrast, the massive and oolitic Mn ores and siliceous limestones preserved the pristine geochemical signatures of the Middle–Late Permian seawater characterized by distinctly low ($^{87}\text{Sr}/^{86}\text{Sr}$)_i and high $\epsilon_{\text{Nd}}(t)$ values. These data indicate a strong impact of the early-stage submarine eruptions of the ELIP on the marine environment in South China and worldwide, likely through intensive seawater–rock interaction.

Keywords: Zunyi manganese; marine chemical sediments; Nd isotope; early stage of the ELIP; Guadalupian extinction



Citation: Yan, H.; Pi, D.; Xu, L.; Sun, K. The Perturbation of the Guadalupian Marine Environment Triggered by Early-Stage Eruption of the Emeishan Large Igneous Province: Rare Earth Element and Sr-Nd Isotope Evidence from Zunyi Manganese Deposit, South China. *Minerals* **2023**, *13*, 965. <https://doi.org/10.3390/min13070965>

Academic Editors: Alexey V. Ivanov, Kejun Hou and Yanhe Li

Received: 7 April 2023

Revised: 7 July 2023

Accepted: 15 July 2023

Published: 20 July 2023



Copyright: © 2023 by the authors. Licensee MDPI, Basel, Switzerland. This article is an open access article distributed under the terms and conditions of the Creative Commons Attribution (CC BY) license (<https://creativecommons.org/licenses/by/4.0/>).

1. Introduction

The Permian Emeishan large igneous province (ELIP) in South China has been proposed to be at least partially responsible for the Guadalupian mass extinction [1–6]. Previous examinations of ELIP’s impact on the paleo-marine environment are mainly focused on the later eruptive phases of terrestrial flood basalts and silicic rocks due to their strikingly large volume [4,7–9]. However, based on high-precision radiometric and biostratigraphic dating constraints, the earlier subaqueous eruptive phases of pillow basalts with mafic submarine hyaloclastite (tuff), which lie in the *J. altudaensis* zone of the Capitanian Stage [10,11] with radiometric ages of ~262 Ma [12,13], temporally fit the Guadalupian oceanic mass extinction [6,14,15]. Therefore, it is necessary to seek reliable proxies that provide various information on seawater composition during the Capitanian Stage to test the effects of early-stage ELIP volcanism.

Previous studies have used the carbon isotope ($\delta^{13}\text{C}$) and strontium isotope ($^{87}\text{Sr}/^{86}\text{Sr}$), both of which have a negative excursion from the carbonate of South China, to reflect the influence of this early phase of ELIP volcanism on the seawater system (e.g., [11,16,17]). In

addition, rare earth elements and yttrium (REY) in a variety of marine chemical sediments (e.g., fish debris, carbonates, manganese formations, and banded iron formations) have also been used as the robust seawater proxies. The close similarity between these sedimentary rocks and the REY distribution pattern in modern seawater can provide the possibility of evaluating the chemical composition and the physico-chemical conditions in ambient seawater from which they formed (e.g., [18–22]).

Another viable proxy is the Sm-Nd isotope system, which provides information on the source(s) of REY in chemical sediments and, therefore, ancient seawater [23–29]. ELIPs always carry a distinct Nd signature compared to the average continental crust and thus might have left a distinct imprint on the seawater record [3]. Additionally, the Sm-Nd isotopic system is resistant to diagenesis and metamorphism during post-deposition [26,27]. Therefore, Nd isotopic variations of marine chemical sediments should reflect source changes. However, no previous studies have focused on the Nd isotope composition of Guadalupian seawater in South China, and there is a lack of perspective regarding what influence the ELIP may have had on the region.

The Zunyi manganese deposit is located in the southwestern Yangtze Platform, South China. The Mn-rich units are hosted in the silicified limestone series in the upper part of the Maokou Formation around the Guadalupian–Lopingian boundary (G–LB) [30–32]. The age of the Zunyi Mn deposit was constrained by the U-Pb dating of zircons from mafic volcanic ash beds in the hanging and foot walls of the Zunyi Mn ore beds, which yielded an age of ~262 Ma [13], corresponding to the *J. altudaensis* biostratigraphic zone of the Capitanian Stage. Therefore, the Zunyi Mn deposits lie on an isochronous horizon with the early-stage subaqueous eruption of the ELIP in South China.

Several studies have proposed that the Zunyi Mn ores are marine chemical precipitates [31] and are formed by microbially-mediated mechanisms [33], therefore providing an ideal and potential target for examining the Nd isotopic composition of seawater in South China during the early stage subaqueous ELIP eruption. In this study, we report major and trace element compositions, especially rare earth elements and yttrium, and Sr-Nd isotopes of samples from the Zunyi Mn deposits to test the reliability of REY on the reflection of seawater composition. We subsequently evaluate the regional isotopic evolution of Nd in Guadalupian seawater in South China. Based on these examinations, we suggest that the early subaqueous eruption of ELIP profoundly affected the Guadalupian marine paleoenvironment in South China, supporting the link between this early-stage volcanism and the Guadalupian biotic crisis.

2. Geological Setting

2.1. Emeishan Large Igneous Province

South China evolved as an isolated continental block during the Permian that occupied tropical latitudes in the eastern Paleo-Tethyan Ocean with the Panthalassa Ocean to the east (Figure 1) [34]. A shallow-water carbonate platform was developed during the Early Permian to Middle Permian [35]. Across the G–LB, an area of ~250,000 km² in South China (Figure 2a) [36] was covered by the ELIP over an estimated duration of ~4 Ma (~263–259 Ma), constrained by bio- and magneto-stratigraphy [37] and geochronology [3]. The early stage (stage 1) of this igneous province consists of voluminous subaqueous pillow basalts with submarine mafic hyaloclastites deposited at ~262 Ma [13] in the *J. altudaensis* conodont zone, Capitanian Stage [10]. Zhu et al. [6] implicated an emergent volcanic system developed in a continental subaqueous rift environment as a consequence of back-arc extension related to the subduction of the Paleo-Tethys oceanic crust beneath the Yangtze plate. Subsequently, an even larger volume of terrestrial flood basalts (stage 2) and silicic rocks (stage 3) were deposited between 260 and 259 Ma that characterize the later eruptive phases (e.g., [3]). The later phase eruption was closely related to the impingement of a mantle plume on the already extant rift system, resulting in the emplacement and distribution of volcanic rocks over a vast region of the western Yangtze plate (e.g., [6]).

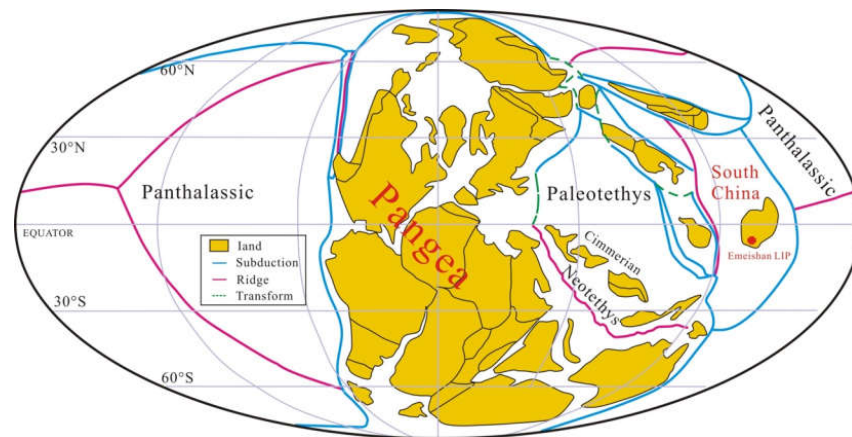


Figure 1. Global palaeomagnetic plate reconstruction at ~262 Ma (adapted from [34]).

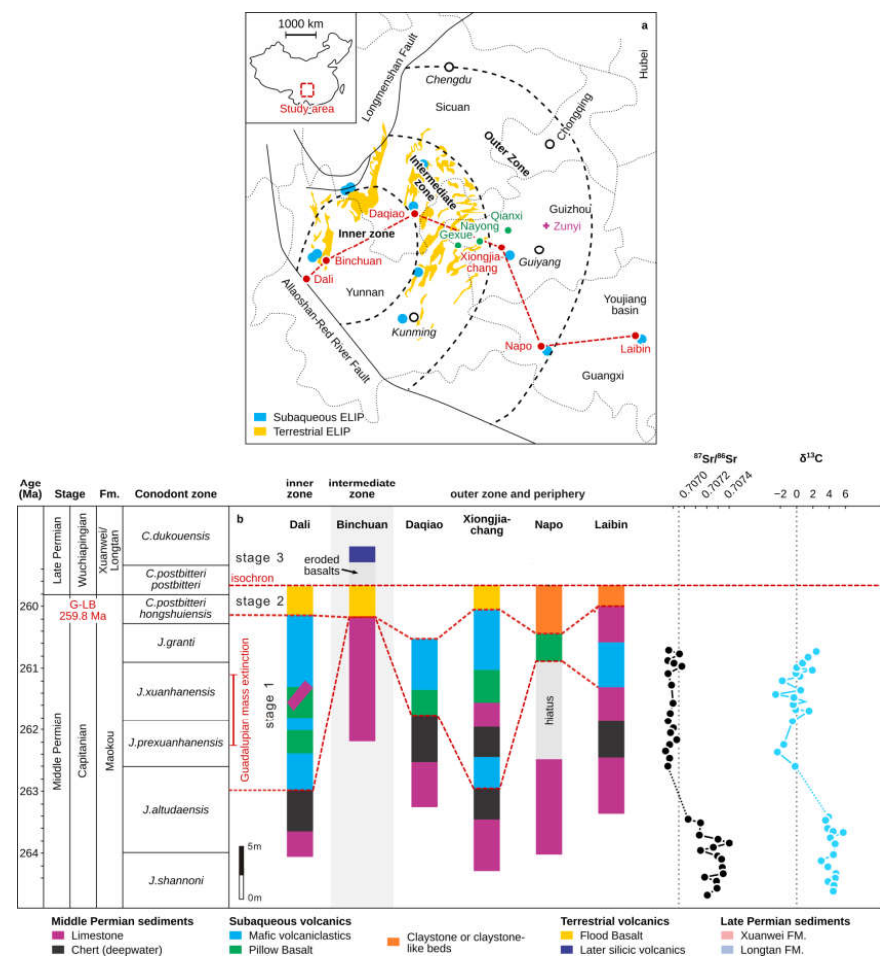


Figure 2. (a) Distribution of Guadalupian–Lopingian boundary (G-LB) sections in the concentric inner, intermediate, and outer zones around the hypothesized core of surficial uplift (modified from [16,38]). The dashed lines indicate the boundaries of the three Emeishan Large Igneous Province (ELIP) zones. Bold italic text: names of the provinces; hollow circles: locations of the respective provincial capitals; red circles: relevant sections taken from the literature and described in the paper; green circles and purple polygons: the locations of studied regions of the manganese deposits reported by [31]. (b) Comparison of the sedimentary record across the G-L interval in the ELIP center to the periphery (beyond ~100 km; corresponding to the red circles in the left panel). Standard international conodont biozones [12] and the Guadalupian mass extinction is marked on the left side of the panel. Carbonate carbon and strontium isotope curves for South China are from [11,17].

As a result of the Emeishan volcanism, the carbonate platform formed inner, intermediate, and outer sedimentary zones: (Figure 2a) [38]. Voluminous subaqueous mafic hyaloclastite deposits from the early-stage ELIP eruption (~262 Ma) [13] are widespread throughout this region (Figure 2b). Such large-scale volcanic activity may have perturbed the paleo-environment through the massive release of magmatic gases, such as SO₂ and CO₂, which could drive cooling on a timescale of years and trigger oceanic anoxia, respectively [39]. These perturbations are possibly reflected by a deeply negative δ¹³C excursion recorded in contemporaneous sedimentary rocks in South China (Figure 2b) [11]. Meanwhile, another highly distinct geochemical feature in the Permian is the progressive and prominent decrease in ⁸⁷Sr/⁸⁶Sr ratios through the Early–Middle Permian that reaches a Paleozoic minimum around the *J. altudaensis* and *J. xuanhanensis* zones of the late Capitanian (Figure 2b) [17].

2.2. Deposit Description

A drowning event in the Middle Permian resulted from the subsidence of the restricted shallow-water carbonate platform on the Yangtze plate during the Emeishan volcanism [37]. Because the shallow water carbonate platform depressed unevenly, NE-direction deepwater platform gullies were formed, such as the one from Zunyi to Nayong (Guizhou Province) and Geyun (Yunnan Province) (Figure 3a). These depressions are ~25–35 km in width, ~300 km in length, and ~60 m deep, and likely controlled the formation and spatial distribution of the Late Permian manganese ore-rich deposits in South China. Tellingly, a suite of siliceous limestones developed along the bottom of the Mn beds in the platform gully [31]. These siliceous limestones clearly differ from the carbonates of the shallow-water platform sedimentary facies that are present on either side of the gully.

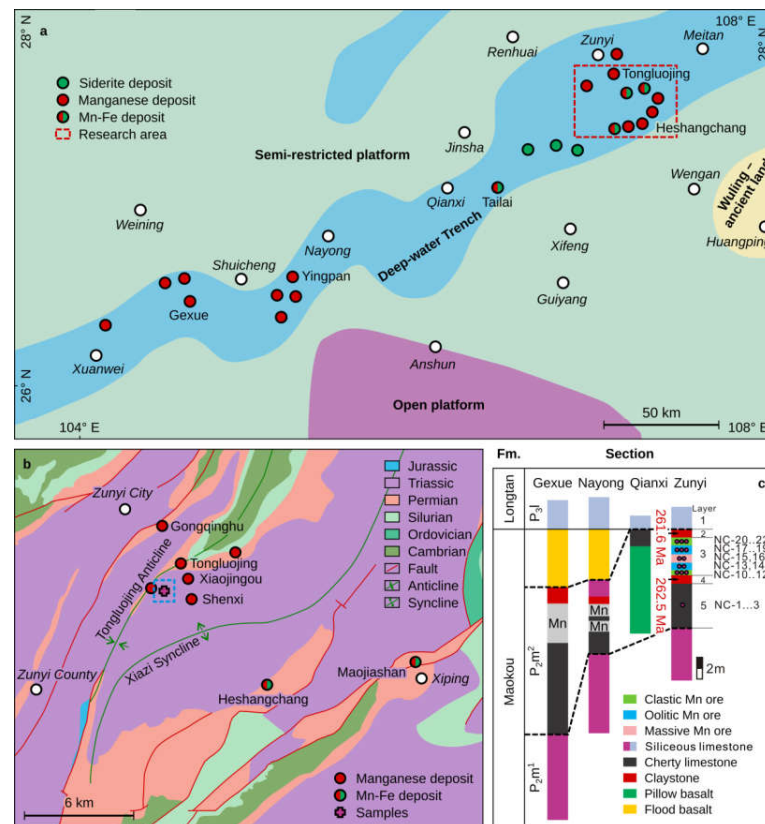


Figure 3. (a) Map showing lithofacies distribution and paleogeography during the late Maokou Stage of the Middle Permian in central-western Guizhou (modified from [31]). (b) Regional geological map of Permian sedimentary manganese deposits in the Zunyi region (modified from [31]). (c) Stratigraphic section for the mafic tuffs and Mn-containing sequence in the Zunyi region [31]; stratigraphic locations of samples for this study are given on the column for the Zunyi locality.

The Zunyi Mn deposit in the northern Guizhou Province is located in the outer zone of the ELIP and within the northeastern gully (Figure 3a). It contains Permian sediments of the Maokou (P_{2m}), Longtan (P_{3l}), and Changshing (P_{3c}) formations, in ascending order. However, there is a lack of strata from the Lower Permian and, possibly, part of the Middle Permian (Figure 3b). The Mn ore bodies are often distributed along the limbs of an anticline that runs in an NNE direction, or occur in superposition to several anticlines (Figure 3b). The Maokou Formation is composed of bioclastic limestones in the lower part and siliceous limestones in the upper part, the latter of which record the lowest $^{87}\text{Sr}/^{86}\text{Sr}$ value in the Permian (Figure 3c) [17]. The Longtan Formation can be subdivided into a lower argillaceous limestone and a coal-bearing upper limestone with a thickness of ~110–120 m. The Changshing Formation exceeds 65 m in thickness and is composed of limestone beds. The Late Permian Zunyi Mn deposits are located between the Maokou and Longtan Formations at the G-LB, stratigraphically equivalent to the regional claystone/mudstone beds that characterize the outer ELIP zone. The mineral composition of the Mn ores is relatively simple, with the main Mn-bearing minerals being rhodochrosite, followed by Mn-rich calcite [32].

A typical Mn-ore-bearing section exposed in an inclined shaft at the Nancha Mn ore mining district, ~12 km south of Zunyi City, is described in detail below. From base to top, five layers were identified (Figure 3c), including:

Layer 1: Mostly siliceous limestones, the upper part of Maokou Formation, locally referred to as the “Bainitang layer”, with a thickness over 10 m.

Layer 2: Lower mafic tuff, corresponding to the footwall of the Mn ore. This layer is 0–0.7 m (average ~0.5 m) thick.

Layer 3: The Zunyi Mn ores, which can be divided into three ore types: (i) massive Mn ores, which occur as a 0.5–1 m thick layer in the middle of the Mn-bearing section. This is the highest-grade (MnO ~38 wt.%) [31] ore and lacks clay materials and pyrites. (ii) Oolitic Mn ore is presented both overlying and underlying the massive ore. The sizes of the oolites are uniform, 1 mm in diameter, and the corresponding ore bodies are about 2 m thick. Rare clay materials, pyrites, and carbonates are also present. (iii) Clastic Mn ores are presented in the lower and upper parts of the Mn-bearing section. These ore bodies are gray-black, with a clastic-pisolitic structure, and have the lowest grade. The pisolites range from 5 mm to 2 cm, and are dominated by Mn-bearing minerals, pyrites, and a variety of clay materials. The pisolites are filled by calcite. The thickness of these ore bodies is about 2–3 m (Figure 4).



Figure 4. Hand specimens of massive (a), oolitic (b), and clastic (c) Zunyi Mn ores, respectively.

Layer 4: The upper mafic tuff, containing pyrite in various abundance. This layer is the hanging wall of the Mn ore; thickness ranges from ~0 to 5.0 m with an average of 2 m.

Layer 5: Argillaceous limestones, representing the lower part of the Longtan Formation. A coal bed was occasionally observed at the base; thickness exceeds 5 m.

3. Materials and Methods

A total of sixteen samples were collected from the No. 2 mine (27°37′38.5″ N, 106°55′49.3″ E) in the Nancha Mn ore mining district, Zunyi City, Guizhou Province, South China, for this study. The samples include three siliceous limestones samples (NC-1, NC-2, and NC-3) from the wall rocks of the upper Maokou Formation, two massive Mn ores (NC-15 and NC-16), five oolitic Mn ores (NC-13, 14, and NC-17–19), and six clastic Mn ores (NC-10–12 and NC-20–22), all collected from Mn ore bodies along a transect from the base to the top. This new set of samples will be compared with the mafic tuffs that represent the altered mafic eruptive rocks from the early stage of the ELIP [13].

The samples for whole-rock geochemical analyses were pulverized to a 200-mesh powder using an agate mill. Major and trace elements were measured using X-ray fluorescence spectrometry (XRF) and inductively coupled plasma mass spectrometry (ICP-MS), respectively, at the Testing Center of Shandong Bureau, China Metallurgical Geology Bureau. Briefly, about 50 mg of powdered sample was dissolved in high-pressure Teflon bombs using an HF + HNO₃ mixture; Rh was used as an internal standard to monitor signal drift during an analytical session for ICP-MS. The USGS rock standards GSP-1 were used for calibrating the element concentrations of the measured samples. The accuracy was estimated to be within 5% for major elements and 10% for trace elements at a confidence level.

Strontium and Nd isotopic compositions were measured using a Finnigan Triton TI thermal ionization mass spectrometer (TIMS) at the State Key Laboratory for Mineral Deposit Research, Nanjing University, following the procedures of Pu et al. [40]. Samples of about 50 mg were dissolved in the same manner as described above for trace element analyses. Complete separation of Sr was achieved by a combination of cation-exchange chromatography in H⁺ form and pyridinium form with the DCTA complex. Nd was separated from the REE fractions by cation-exchange resin using HIBA as an eluent. After purification, the separated Sr was dissolved in 1 µL of 1 N HCl and then loaded along with a TaF₅ solution onto tungsten filaments for ⁸⁷Sr/⁸⁶Sr analysis on TIMS. The separated Nd was dissolved in 1 µL of 1 N HCl and then loaded with a H₃PO₄ solution onto Redouble filaments for ¹⁴³Nd/¹⁴⁴Nd analysis on TIMS. The ⁸⁷Sr/⁸⁶Sr and ¹⁴³Nd/¹⁴⁴Nd ratios are reported normalized to the natural ⁸⁶Sr/⁸⁸Sr ratio of 0.1194 and ¹⁴⁶Nd/¹⁴⁴Nd ratio of 0.7219, respectively. During the period of laboratory analysis, measurements of the Sr standard NIST SRM-987 yielded an ⁸⁷Sr/⁸⁶Sr ratio of 0.710252 ± 16 (2σ, n = 12), similar to the reference value, and measurements of the JNdi-1 Nd standard yielded a ¹⁴³Nd/¹⁴⁴Nd ratio of 0.512121 ± 6 (2σ, n = 12), which is similar to the reference value of 0.512115 ± 7 [41]. The total analytical blanks were 50 pg for Sm and Nd and 0.2–0.5 ng for Rb and Sr.

4. Results

4.1. Major and Trace Elements

The major and trace element concentrations of the Zunyi Mn ores and the siliceous limestones are presented in Supplementary Table S1. The concentrations of MnO in the oolitic and massive Mn ore samples range from 45.09 to 72.35 wt.%, which are higher than those of the clastic Mn ores (26.04 to 32.24 wt.%). Siliceous limestones, oolitic Mn ores, and massive Mn ores have low Al₂O₃ (0.60 to 1.57 wt.%) and TiO₂ contents (0.10 to 0.29 wt.%) (Figure 5a). However, clastic Mn ores contain Al₂O₃ (6.28% to 9.80 wt.%) and TiO₂ (0.34 to 0.84 wt.%) four times higher than the oolitic or massive Mn ores (Figure 5a).

All of the Zunyi Mn ore and siliceous limestone samples display a wide range of contents for the immobile trace elements (e.g., Sc, Zr, Th, and Hf), which are reliable tracers to evaluate the potential impact of detrital aluminosilicates (e.g., [18]). Siliceous limestone, oolitic Mn ore, and massive Mn ore samples contain 0.72 to 1.69 ppm Sc, 16.50 to 37.00 ppm Zr, 0.35 to 0.89 ppm Th, and 0.25 to 0.95 ppm Hf. These values are much lower than those of the clastic Mn ore samples (Table S1, Figure 5b,c).

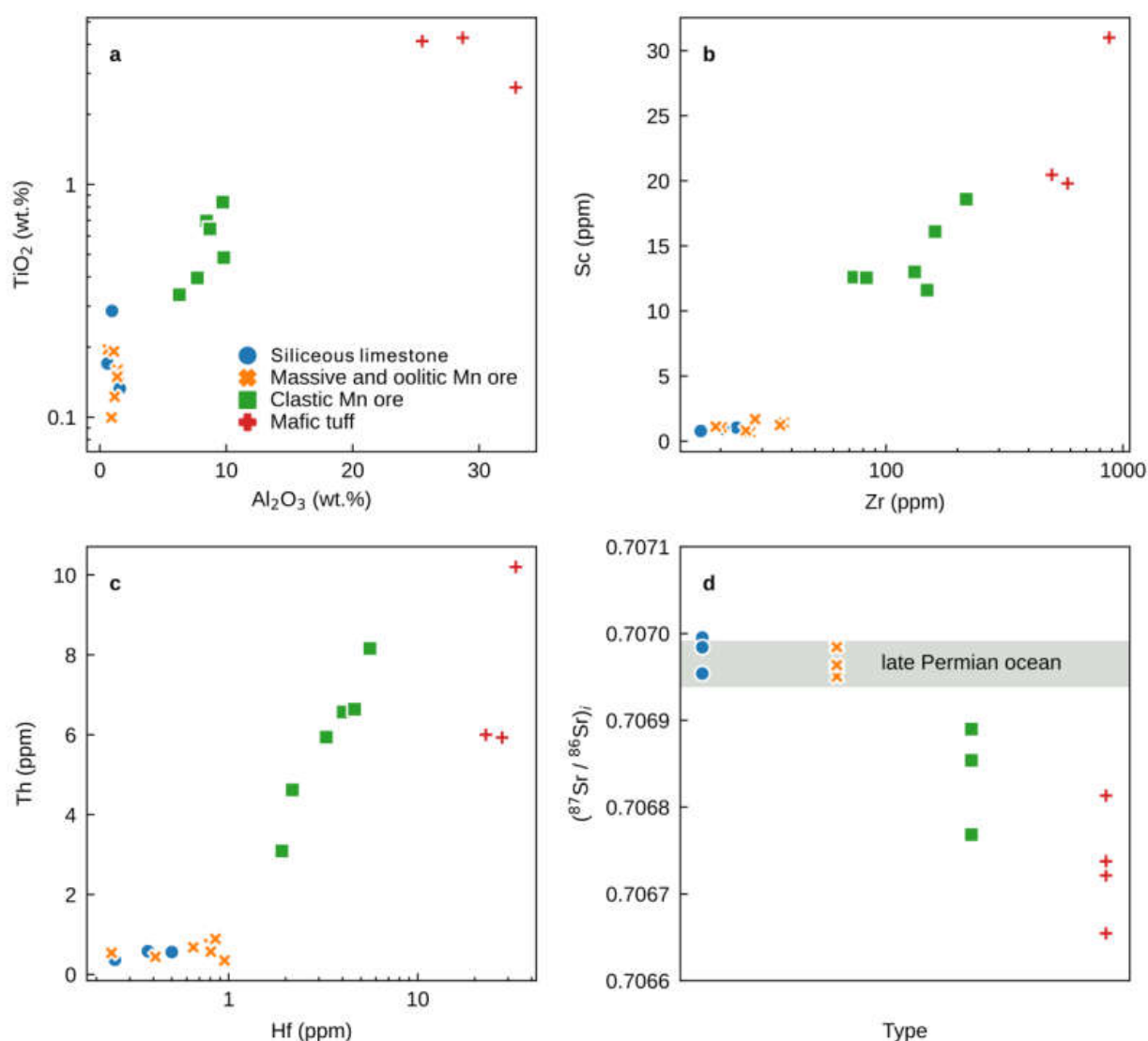


Figure 5. Bivariate plots of (a) TiO_2 (wt.%) and Al_2O_3 (wt.%), (b) Sc (ppm) and Zr (ppm), (c) Th (ppm) and Hf (ppm), and (d) $^{87}\text{Sr}/^{86}\text{Sr}_I$ for the massive, oolitic, and clastic Mn ores and siliceous limestones from the upper Maokou Formation in the Nancha section, northern Guizhou Province, South China. Data for the mafic tuffs (claystone) from the foot and hanging wall of the Nancha Mn ores are from [13]. $^{87}\text{Sr}/^{86}\text{Sr}_I$ composition for the Late Permian global ocean from [17]. Clastic Mn ore samples are characterized by lower $^{87}\text{Sr}/^{86}\text{Sr}_I$, higher Al_2O_3 , TiO_2 , Th, Hf, and Sc concentrations and positive correlations.

The post-Archean Australian shale (PAAS)-normalized ('SN' suffix) REY (REY_{SN}) distribution patterns in all of our samples display two distinct trends coupling with their Al_2O_3 contents (Table S2; Figure 6). The siliceous limestone, oolitic Mn, and massive Mn ore samples, which are characterized by low Al_2O_3 contents, all exhibit depletions in light REE (LREE_{SN}) relative to heavy REE (HREE_{SN}) ($\text{La}_{\text{SN}}/\text{Yb}_{\text{SN}} = 0.69\text{--}0.90$), positive La ($\text{La}_{\text{SN}}/\text{La}_{\text{SN}}^* = 1.12\text{--}3.80$; asterisk refers to concentration expected from neighboring elements; $\text{La}/\text{La}^* = \text{La}_{\text{SN}}/(3\text{Pr}_{\text{SN}} - 2\text{Nd}_{\text{SN}})$) and Gd ($\text{Gd}_{\text{SN}}/\text{Gd}_{\text{SN}}^* = 1.03\text{--}1.10$; $\text{Gd}/\text{Gd}^* = \text{Gd}_{\text{SN}}/(0.33\text{Sm}_{\text{SN}} - 0.67\text{Tb}_{\text{SN}})$) anomalies, negative Ce ($\text{Ce}_{\text{SN}}/\text{Ce}_{\text{SN}}^* = 0.38\text{--}0.48$; $\text{Ce}_{\text{SN}}/\text{Ce}_{\text{SN}}^* = \text{Ce}_{\text{SN}}/(0.5\text{La}_{\text{SN}} + 0.5\text{Pr}_{\text{SN}})$) anomalies, and elevated Y/Ho ratios (38.93–58.11). In striking contrast, the clastic Mn ore samples characterized by relatively high Al_2O_3 contents show positive Ce anomalies ($\text{Ce}_{\text{SN}}/\text{Ce}_{\text{SN}}^* = 1.07\text{--}1.42$) and sub-chondritic Y/Ho ratios (20.63–25.12). All samples show the negative Eu ($\text{Eu}_{\text{SN}}/\text{Eu}_{\text{SN}}^* = \text{Eu}_{\text{SN}}/(0.5\text{Sm}_{\text{SN}} + 0.5\text{Gd}_{\text{SN}})$) anomalies.

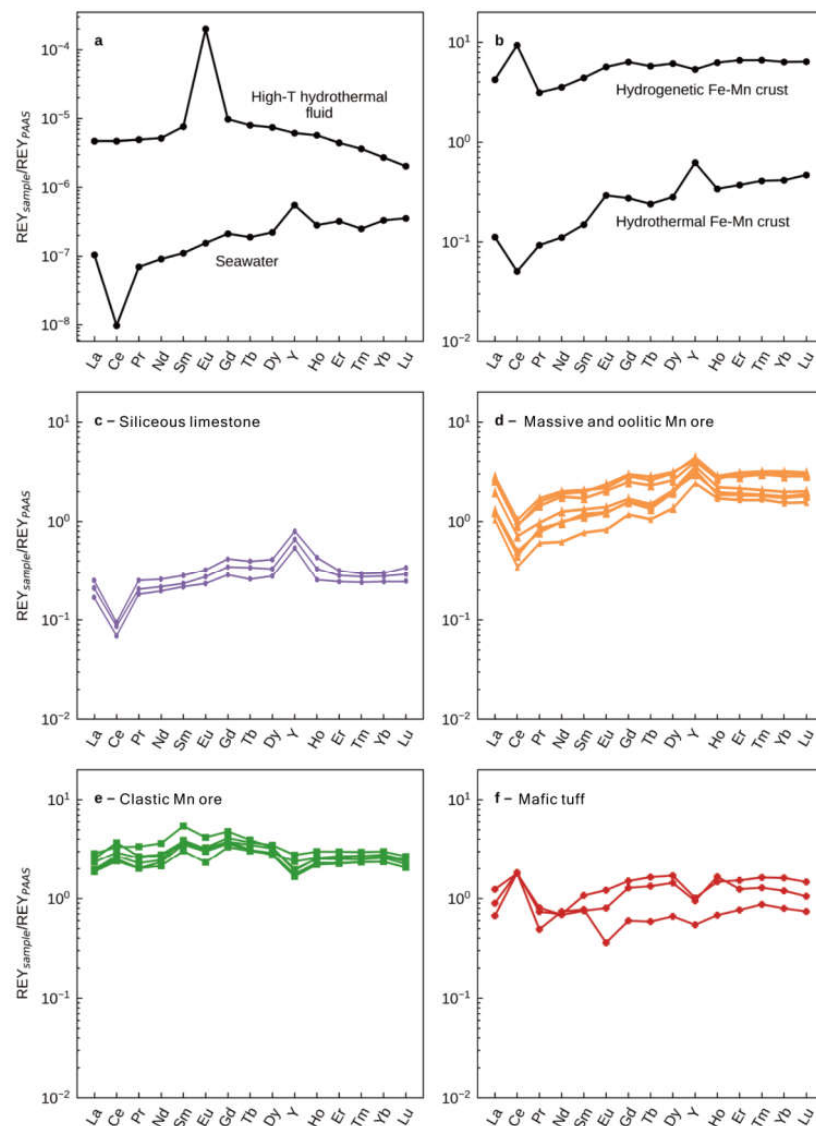


Figure 6. (a) Examples of typical REE + Y_{SN} patterns of high-temperature hydrothermal (black-smoker) fluids [42] and seawater [43]. (b) Examples of typical REE + Y_{SN} patterns of marine hydrothermal Fe-Mn deposits and hydrogenetic Fe-Mn nodules (data from [20]). Post-Archean Australian shale (PAAS)-normalized REE + Y patterns of (c) siliceous limestones, (d) massive and oolitic Mn ores, (e) clastic Mn ores, and (f) mafic tuff from the upper Maokou Formation in the Nancha section, northern Guizhou Province, South China. Mafic tuff data are from [13]. The REE + Y_{SN} patterns of clastic Mn ore samples are similar to the tuffs and display positive Ce anomalies and negative Y anomalies. The REE + Y_{SN} patterns for the massive and oolitic Mn ores and siliceous limestones of the Maokou Formation show LREE depletions, negative Ce, and positive La, Gd, and Y anomalies that are similar to those observed in modern seawater.

4.2. Sr-Nd Isotopes

The strontium and Nd isotopic compositions are listed in Tables S3 and S4, respectively. The siliceous limestone, oolitic Mn ore, and massive Mn ore samples have a similar and narrow range of $^{87}\text{Sr}/^{86}\text{Sr}_i$ from 0.706950 to 0.706995 (Figure 5d), but the $^{87}\text{Sr}/^{86}\text{Sr}_i$ values of the clastic Mn ore samples are lower (0.706769–0.706890) (Figure 5d). Neodymium isotopes were only measured on siliceous limestone, oolitic Mn ore, and massive Mn ore samples with low Al_2O_3 contents. The $\epsilon_{\text{Nd}}(t)$ values across these lithologies are consistently low with a narrow range from -2.4 to -3.2 (Figure 7a).

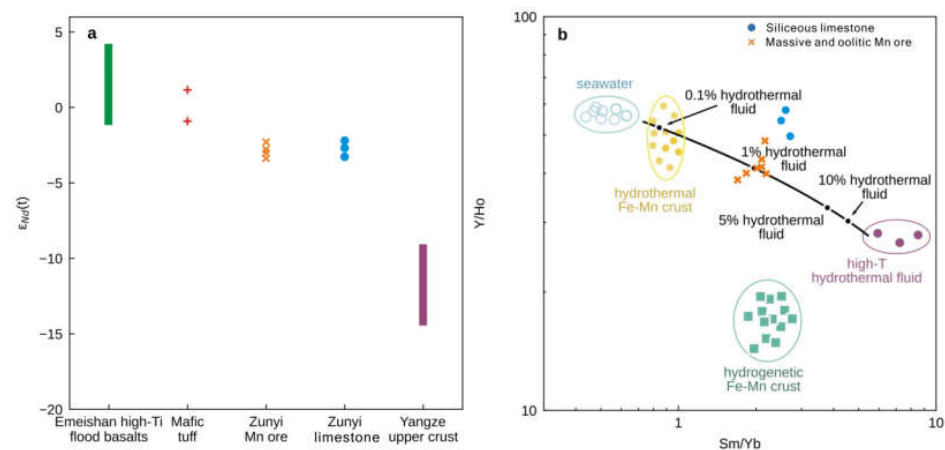


Figure 7. (a) Comparison of $\epsilon_{Nd}(t)$ between different lithologies studied here and those characteristic of the Yangtze Block [44,45], mafic tuff [13], and Emeishan flood basalts [3]. (b) A two-component conservative mixing line between seawater and high-temperature hydrothermal fluids, plotted on a Y/Ho versus Sm/Yb bivariate plot, showing that a 1% high-temperature hydrothermal (>350 °C, [18]) fluid contribution to seawater [42] is sufficient to explain Sm/Yb ratios in the siliceous limestones and massive and oolitic Mn ore samples from this study.

5. Discussion

5.1. Depositional Controls on REY in the Zunyi Mn Deposit

It is possible that the REY concentrations of the Zunyi Mn ores have been affected by several processes, including: (1) syn- and post-depositional processes; (2) the degree to which the REY were scavenged by particulate matter in the water column prior to deposition; and (3) also by other inputs to the seawater from which the Mn ores precipitated.

5.1.1. Syn-Depositional Detrital Contamination

During the syn-depositional stage, REY_{SN} patterns in chemical precipitates could be modified from the signature of contemporaneous seawater due to contamination by detrital aluminosilicates. The relative contribution of detrital input can be assessed by examining the abundances of immobile high-field strength elements in aqueous solution, such as Al, Ti, Zr, Hf, Th, and Sc (e.g., [46,47]). Elevated abundances of these elements are unlikely to have derived from seawater, so they serve as indicators of clastic detrital contamination in chemical sediments. In Figure 5a–c, the Al₂O₃, TiO₂, Th, Hf, and Sc contents of the clastic Mn ore samples are the highest among all of the samples analyzed in this study, but lower than the mafic tuff analyzed by Yan et al. [13], which serves as an aluminosilicate-rich end-member derived entirely from volcanic material. Positive correlations between Al₂O₃ and TiO₂, Sc and Zr, and Hf and Th were observed in the clastic Mn ore samples, consistent with relatively high detrital input. In contrast, the massive and oolitic Mn ore and siliceous limestone samples are characterized by lower abundances of high-field strength elements. Positive correlations between these elements are either weaker or absent. Such characteristics indicate that the massive and oolitic Mn ores are less affected by detrital material.

REY concentrations in hydrothermal fluids and seawater are low, and any admixture of detrital materials would significantly alter the REY_{SN} patterns towards the compositions of the detrital components. The REY_{SN} patterns of the clastic Mn ore samples are similar to those of the mafic tuff of the hanging and foot walls of the Mn ores [13] in displaying distinctive positive Ce anomalies and negative Y anomalies (Figure 6e–f). Conversely, REY_{SN} patterns of massive and oolitic Mn ores and the underlying siliceous limestones from the Maokou Formation show LREE_{SN} depletions, negative Ce anomalies, as well as positive La, Gd, and Y anomalies (Figure 6c–d), which are similar to those of modern seawater (Figure 6a).

The $^{87}\text{Sr}/^{86}\text{Sr}_i$ ratios of massive and oolitic Mn ore samples are indistinguishable from the values of the siliceous limestones and the value of the Middle–Late Permian seawater (Figure 5d; [17]). In contrast, the $^{87}\text{Sr}/^{86}\text{Sr}_i$ ratios of the clastic Mn ores samples (mean 0.706837) are much lower, approaching the very low values of the mafic tuff from the hanging and foot walls of the Zunyi Mn ores (0.706729; [13]), which again indicates that the detrital component has influenced the $^{87}\text{Sr}/^{86}\text{Sr}$ ratios of the clastic Mn ore samples (Figure 5d). In light of the geochemical considerations presented above, we infer that only the REY in the massive and oolitic Mn ores, along with the siliceous limestone samples, are reliable archives of ancient marine geochemical signatures, whereas the clastic Mn ore samples have been geochemically altered by the influx of detrital aluminosilicates.

5.1.2. Post-Depositional Alteration

The main Mn-bearing minerals in the Zunyi Mn deposit are rhodochrosite (MnCO_3) and kutnohorite ($\text{CaMn}(\text{CO}_3)_2$) [31]. Based on carbon isotope data and detailed petrographic observations [30,32], the presence of Mn(II)-carbonates was attributed to the reduction of primary Mn(III/IV) oxyhydroxides coupled to the oxidation of organic matter in the anoxic sediment column during the diagenetic stage. Thus, during the process, the REY accumulation can likely be controlled by two mechanisms: (i) absorption onto primary Mn oxyhydroxides from the water column and (ii) post-depositional alteration, i.e., release from organic matter.

Due to the lack of metamorphism records in the studied region, the potential post-depositional mechanisms affecting REY distribution in the Zunyi Mn deposit are diagenetic processes, where the REY accumulation may also be modified by the release from organic matter in porewater. The REY_{SN} patterns of the rocks and minerals, which are associated with organic matter decay during diagenesis, are characterized by the pronounced enrichment of middle rare earth elements (MREE_{SN}), producing a “hat-shape” REY_{SN} distribution pattern, such as the Early Cambrian black shales of Guizhou province [48], phosphorites hosted in the lower Cambrian Series of Yunnan province [49], phosphatic nodules hosted in the Niutitang Formation of Western Hunan [50], phosphatic rocks hosted in the Neoproterozoic Ediacaran Doushantuo Formation of Western Hubei [51], and some fossil organisms [52]. However, the REY_{SN} patterns of the massive and oolitic Mn ore samples in this study are inconsistent with the “hat shape” patterns, suggesting a negligible contribution of REY from organic matter during the early diagenetic stage in the Zunyi Mn ores. In addition, CeO_2 produced by oxidation soluble Ce^{3+} in oxic marine environments also tends to be rapidly removed from seawater via scavenging by organic matter in suspension [53,54]. In suboxic/anoxic porewater environments, insoluble CeO_2 would be reduced to soluble Ce^{3+} during the remineralization of organic matter, producing positive Ce anomalies in REE distributions. However, the lack of positive Ce anomalies in the massive and oolitic Mn ores could exclude the influence of organic matter.

In addition, though there is a lack of work on REY remobilization during the diagenesis of Mn deposits, carbonates and iron phases have been assessed for diagenetic immobile REE patterns and no significant effect has been found [18]. Since Mn geochemistry closely resembles that of Fe, REY_{SN} patterns likely also stay relatively unmodified through Mn diagenesis. In our study, this is supported by the presence of highly seawater-like REY_{SN} patterns in our Mn ores and siliceous limestones. However, dedicated studies of REY partitioning through Mn diagenesis are necessary to fully establish Mn deposits as a robust marine REY archive.

5.1.3. Scavenged by Mn Oxyhydroxides from Ambient Seawater

Previous studies have proposed that the absorption of REY from ambient seawater by particulate matter (Mn/Fe oxyhydroxides) precipitated in the oxygenated water column would primarily dominate the REY origin of the ancient metalliferous sediments. Experimental studies [55–58] as well as investigations of natural systems (e.g., [59], and references therein) showed that the partitioning of REY during the precipitation of Mn

oxyhydroxide particles from seawater is not only accompanied by strong fractionation between the solid and the respective solution, but also by distinctive fractionation within the REY group, related with the anomalies for redox-sensitive as well as non-redox sensitive elements. Moreover, this model assumes that the reaction kinetics of adsorption/desorption on REY are significantly faster than the Mn oxyhydroxide particle residence time in an oxic water column. This assumption is supported by experimental evidence indicating that particle-surface/solution REY exchange equilibrium occurs within minutes [42], suggesting that most Mn oxyhydroxide particles settling through an oxic water column (of relatively constant REY distribution) should be in equilibrium with the solution phase (seawater).

Natural systems that provide insight into such equilibrium exchange processes are available in the form of modern marine hydrogenetic manganese crusts that precipitated from seawater as initially colloidal particles within the water column and are characterized by exceedingly slow growth rates and by strong REY enrichments that can exceed 1000 ppm (Figure 6b; e.g., [20]). Patterns of REY_{SN} partition coefficients between marine hydrogenetic Mn crusts and seawater tends to decrease from La to Lu (e.g., [60]). Thus, Mn oxyhydroxide colloidal particles usually preferentially absorb light rare earth elements. In addition, due to the lower stability of surface complexes of Y relative to those of Ho during the redox cycling of Mn, Mn oxyhydroxide particles exhibit the preferential sorption of Ho relative to Y [23,60]. In addition, Ce is a redox-sensitive rare earth element [61]. In oxic marine environments, soluble Ce^{3+} is oxidized into insoluble Ce^{4+} as CeO_2 and tends to be rapidly removed from seawater via scavenging by Mn oxyhydroxides [59]. Consequently, the hydrogenetic Mn crusts and nodules representing the equilibrium between manganese oxyhydroxides and seawater record prominent positive Ce anomalies and negative Y anomalies (Figure 6b).

The existence of Mn oxyhydroxide during the sedimentary stage represents oxygenated bottom water. If scavenging Mn oxyhydroxide particles achieved exchange equilibrium with the surrounding seawater, the above observations would predict positive Ce and negative Y anomalies in the Zunyi Mn deposit. On the contrary, the obvious negative Ce and positive La, Gd, and Y anomalies strongly suggest that Mn oxyhydroxide particles that scavenged REY could not be at or near exchange equilibria with respect to ambient seawater, but similar to the modern seawater pattern of REY_{SN} . This feature is also presented in hydrothermal Mn oxyhydroxide deposits precipitating from marine hydrothermal systems (Figures 6b and 7b; e.g., [20]). When these reducing high-temperature hydrothermal fluids containing substantial amounts of metal ions mix with cold seawater after exiting the seafloor, low-valence manganese is oxidized and precipitated quickly [62–64]. Due to high sedimentary rates, in marked contrast to hydrogenetic crusts, an exchange equilibrium between manganese oxyhydroxides and ambient seawater had not yet been established for those REY elements that form surface complexes on the metal oxyhydroxide surface [20]. Such similar features have also been proposed in the research on REY in manganese ores and BIFs during Precambrian [26,65,66] and Cenozoic hydrothermal manganese ore [20], which are all recognized as faithful proxies to reflect seawater composition. In addition, the higher REY content of Mn ores than siliceous limestones is likely attributed to the continuous uptake of REY from seawater onto Mn oxyhydroxide, even after deposition, until their burial. However, the striking similarity between REY patterns in siliceous limestones and Zunyi Mn ores suggests that massive and oolitic Mn ores as pure chemical sediments faithfully record the REY distributions of contemporaneous seawater. Thus, some general constraints may be placed on the composition of Middle–Late Permian seawater.

5.2. Middle–Late Permian Seawater in South China

5.2.1. Sr Isotopes in the Middle–Late Permian Seawater

The strontium isotopic composition ($^{87}Sr/^{86}Sr$) of marine carbonates provides valuable information about the relative importance of the sources contributing Sr to the seawater [16,17]. The marine Sr isotopic ratio is balanced by input fluxes from the continental crust with radiogenic ^{87}Sr (riverine flux) and Earth's mantle (hydrothermal or other mafic igneous

oceanic crust) [67,68]. $^{87}\text{Sr}/^{86}\text{Sr}$ ratios in marine biominerals appear to be uniform at a global scale because the residence time (>1000 kyr) of Sr in the oceans is longer than the average mixing time of the ocean [69–71]. The lowest $^{87}\text{Sr}/^{86}\text{Sr}$ ratios in the Paleozoic have been reported from the G-LB in Japan, Russia, and South China [15,17,72–74]. Over this period, the $^{87}\text{Sr}/^{86}\text{Sr}$ trend shows a monotonous decline from approximately 0.7080 in the earliest Permian to approximately 0.7069 in the late Capitanian *J. altudaensis* and *J. xuanhanensis* zones, followed by a steeper increase from the latest Guadalupian towards the Permian–Triassic boundary (~0.7071–0.7072) and into the Early Triassic (Figure 2). In South China, compared to the cessation the input of terrigenous material enriched in radiogenic Sr, this short-lived $^{87}\text{Sr}/^{86}\text{Sr}$ excursion is best interpreted to reflect an enhanced ELIP mantle-derived hydrothermal flux into seawater with an additional minor contribution from ELIP-related volcanism [16].

5.2.2. A Hydrothermal Input?

REY_{SN} distribution patterns of the Zunyi Mn ores show relative LREEs enrichment with higher Sm_{SN}/Yb_{SN} ratios (0.69–0.90) than those of modern shallow seawater (0.21–0.50), likely suggesting that other sources of REY with enriched LREE_{SN}, such as hydrothermal fluid, could have added in the ambient seawater. REY_{SN} patterns of marine high-temperature hydrothermal fluids are characterized by relative LREE_{SN} enrichment and notable positive Eu anomalies (Figure 6a; [42]). Most carbonates influenced by hydrothermal fluid show positive Eu anomalies. However, in this study, all samples show no positive Eu anomaly, seemingly not supporting the influence by hydrothermal fluids. Because Eu³⁺ reduces to Eu²⁺ under reducing conditions [61], under high temperatures (greater than 250 °C) and high pressures, divalent Eu predominates, and hydrothermal fluids and sediments of hydrothermal origin are usually characterized by their obvious positive Eu anomalies [43,75]. When reducing, high-temperature hydrothermal fluids migrated from the source far away, oxic, low-temperature seawaters will be mixed, leading to the substantial drop in temperature and changes in redox condition. Therefore, the positive Eu anomaly from hydrothermal fluid is locally preserved, which could well be interpreted as REY_{SN} patterns of low-temperature hydrothermal fluids having no positive Eu anomalies. Hence, sediments with no positive Eu anomalies are not absolutely excluded from the influence of hydrothermal fluids. However, the presence of the higher Sm/Yb ratios and slightly lower Y/Ho values does indeed tend to have at least some input from ‘black smoker’ type hydrothermal fluids (Figure 7b). The Y/Ho ratio of modern seawater is 44–74 [42], and small admixtures of any contaminant would reduce the Y/Ho ratio of seawater towards the value of the upper continental crust ~27.5. Generally, seawater has high Y/Ho (~60) and low Sm/Yb (~0.8) ratios, while high-temperature hydrothermal fluids have low Y/Ho (~27) and high Sm/Yb (~8) ratios [42]. A two-end member mixing modeling based on the Sm/Yb and Y/Ho data yielded a lower contribution of ~1% from high-temperature hydrothermal fluids to the Zunyi Mn ores and siliceous limestones (Figure 7b). This calculation is comparable with the model of Klein and Beukes [76], who noted that a 100:1 mixing ratio of typical North Atlantic seawater with deep-sea hydrothermal fluids produced REY_{SN} patterns. Therefore, the contribution from hydrothermal fluids to the Middle–Late Permian seawater appears minimal. Generally, the Sr isotope of riverine inputs with radiogenic (high) $^{87}\text{Sr}/^{86}\text{Sr}$ ratios (average ~0.7119) and of mantle-derived high-temperature hydrothermal inputs at the mid-ocean ridges with unradiogenic (low) $^{87}\text{Sr}/^{86}\text{Sr}$ ratios (average ~0.7035). Thus, hydrothermal fluids could be insufficient as a main mechanism to result in the low $^{87}\text{Sr}/^{86}\text{Sr}$ ratios of our samples, even the contemporaneously negative Sr excursion record. In addition, we propose that Nd in Zunyi Mn ores and siliceous limestone was mostly derived from ambient seawater rather than hydrothermal input and would thus be expected to record the Nd isotopic composition of this seawater.

5.2.3. Nd Isotopes in the Middle–Late Permian Seawater

The neodymium isotopic compositions of Earth’s crust and mantle have diverged since the development of the earliest continental crust [77]. The fractionation of Sm–Nd by partial melting triggered the retention of Sm in the residual mantle and the partitioning of Nd into the melt. $^{143}\text{Nd}/^{144}\text{Nd}$ in marine sediments is also mass balanced by Nd inputs from the continents via the riverine flux and the mantle via the hydrothermal leaching or weathering/hydrolysis of mafic igneous oceanic crust [78]. Neodymium isotope studies of Archean seawater have shown that the Nd originate almost combines between continental sources and mantle sources, including black-smoker-type high-temperature hydrothermal fluids (e.g., [78,79]). Unlike the Sr isotope system, however, the effect of local hydrothermal venting of Nd on the Phanerozoic marine signal is not considered significant. Although hydrothermal vent fluids have Nd concentrations more than 500 times greater than seawater, the buoyant plume will be diluted quickly (within an hour) to 1/10,000th of its initial concentration across a distance of less than 1 km when mixed with seawater [80]. In addition, Nd sourced from hydrothermal vents is scavenged by hydrothermal polymetallic oxyhydroxides particles very close to or even within the hydrothermal system, whereas the scavenging is disproportionate and unpredictable [81]. Therefore, in generally oxic Phanerozoic oceans, hydrothermal vent fluids have a negligible effect on the Nd isotopic composition of seawater and distal Fe- and Mn- marine sediments. In general, an increasing $^{143}\text{Nd}/^{144}\text{Nd}$ trend indicates a higher contribution of mantle-derived Nd, and a decreasing trend indicates an increased contribution from the continental crust. Finally, due to its high ionic potential, Nd is a particle-reactive element and its residence time in modern seawater is, therefore, relatively short (~500–1000 years; [82,83]), which is less than the average mixing time of the ocean [78].

In the Middle Permian ocean, Nd likely had a similar residence time on the order of 10^3 years, suggesting that marine Nd isotope compositions would be spatially heterogeneous. Keto and Jacobsen [84] showed that Middle to Late Permian samples from Alaska and Iran deposited in the Pacific/Panthalassa Ocean (PPO) have much higher $\epsilon_{\text{Nd}}(t)$ values of -3 to -6 , compared to -12 in samples from the earlier Permian and -9 in the Early Triassic (Figure 8). This is attributed to the changes in the rate of crustal additions or the mafic volcanism. In contrast to the modern oceans, where information on the worldwide distribution of seawater $\epsilon_{\text{Nd}}(t)$ is readily available, such a database does not yet exist for the end-Guadalupian ocean in South China.

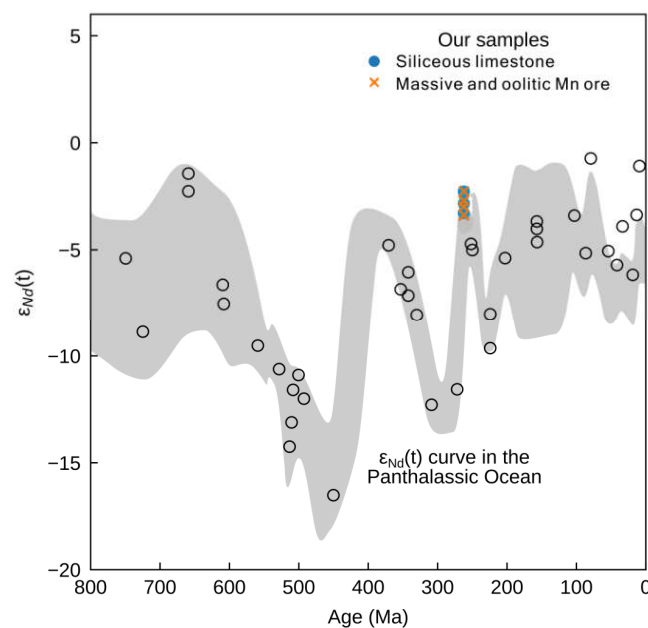


Figure 8. $\epsilon_{\text{Nd}}(T)$ values of siliceous limestones and Mn ore samples from this study superimposed on a curve of contemporaneous values for the Panthalassic Ocean [84].

5.2.4. Nd Isotopes in the Zunyi Mn Deposit

The neodymium isotope composition of the Zunyi Mn deposit offers a way to assess the magnitude and heterogeneity of mantle and crustal contribution to Late Permian marine geochemistry. During the Permian, the upper/middle Yangtze crust was characterized by $\epsilon_{\text{Nd}}(t)$ values < -8 (Figure 7a; [44,45]). In contrast, the mafic tuff in the foot and hanging walls of the Zunyi Mn ores displays values around 0, similar to the Nd isotope composition of contemporaneous Emeishan basalts and consistent with the derivation of this material from the mantle ([3], and references therein). The $\epsilon_{\text{Nd}}(t)$ values of the massive and oolitic Mn ores, as well as the associated siliceous limestones, all display seawater-like REY_{SN} distribution patterns, approaching both the tuff rocks and Emeishan high-Ti flood basalts, but are significantly different from the crustal basement rocks of the Yangtze Block (Figure 7a). Assigning the continental flux an ϵ_{Nd} value of -8 , mass balance calculations suggest that at least 50% of the Nd in these samples must have originated from a source possessing a mantle signature.

The driving mechanism of the Late Permian Nd isotope evolution in South China remains not well constrained. With the minimal contribution of Nd (REY) from hydrothermal fluids to the seawater (discussed in Section 5.2.2), which would only result in insignificant perturbations of the $\epsilon_{\text{Nd}}(t)$ value, the high $\epsilon_{\text{Nd}}(t)$ values for Late Permian seawater in South China are more parsimoniously explained by a major contribution from the contemporaneous Emeishan mafic volcanic rocks. Biostratigraphic and sedimentological constraints suggest the early stage ELIP occurred as submarine eruptions of hyaloclastites [14,37,85] beginning in the *J. altudaensis* conodont zone (~263 Ma; [37]). In subsequent stages, Emeishan flood basalts erupted in continental environments (~260 Ma; [37]) around the G-LB. Therefore, the increase in the $\epsilon_{\text{Nd}}(t)$ ratios of the seawater was likely caused by the release of significant quantities of less radiogenic Nd from intensive hydrolysis of submarine mafic volcanoclastic materials, the signal of which was transferred into the contemporaneous Zunyi Mn deposits.

The neodymium isotopes in the massive/oolitic Mn ore and siliceous limestone samples also match the upper end for late Permian seawater $\epsilon_{\text{Nd}}(t)$ values from the Panthalassic Ocean (Figure 8; [84]), suggesting that a mantle/ELIP-derived component was also globally prevalent, not only in South China. Additionally, our Nd isotopes are a little bit higher than usual for that time, meaning that the Zunyi Mn deposit was closer to the mantle Nd source—e.g., the ELIP may be the driving mechanism of the Late Permian Nd isotope evolution.

6. Potential Link between the Guadalupian Marine Environmental Perturbation and the Early Stage of the ELIP

The widespread existence of voluminous subaqueous pillow basalts associated with mafic submarine hyaloclastite deposits from the early-stage eruption of the ELIP at the *J. altudaensis* biostratigraphic zone has drawn increasing attention as a potential cause of the Guadalupian mass extinction (e.g., [6,13,14]). The submarine eruption of the ELIP may have not only released significant amounts of volatiles (dominantly CO₂ and SO₂) into the seawater to result in volcanogenic ocean warming and acidification [39], and then have caused the Capitanian extinction, but also induced an intensive seawater–basalt interaction to release mantle material, which may result in the chemical property change of seawater.

Our data support this hypothesis by highlighting a major increase in mantle contribution to the seawater Nd isotope budget at ~262 Ma. It suggests that early-stage submarine mafic ELIP eruptions were sufficient to affect the end-Guadalupian marine environment. That high Nd isotope ratios are also common in other contemporaneous Panthalassan sections [84] further hints that this was an event with global repercussions for seawater chemistry.

7. Conclusions

- The clastic Mn ore has been contaminated by mafic aluminosilicates, whereas the massive and oolitic Mn ores, as well as associated siliceous limestones, have not been altered and thus have preserved their pristine signature as chemical sediments.
- The REY_{SN} patterns of the massive and oolitic Mn ores and siliceous limestones are consistent with modern seawater-like patterns, further demonstrating that these samples recorded the geochemical signatures of the end-Guadalupian seawater in South China.
- The $\epsilon_{Nd}(t)$ values for the massive and oolitic Mn ores and the siliceous limestones (−2.4 to −3.2) are relatively high, lying at the high end of the range of global end-Guadalupian seawater values.
- These high $\epsilon_{Nd}(t)$ values result from the input of mantle-derived Nd into seawater by the hydrolysis of contemporaneous subaqueous mafic volcanoclastic materials from the early-stage eruption of the ELIP, which resulted in the chemical property change of contemporaneous seawater in South China.

Supplementary Materials: The following supporting information can be downloaded at: <https://www.mdpi.com/article/10.3390/min13070965/s1>, Table S1: Major oxide (wt.%) and trace element (ppm) compositions of Zunyi samples; Table S2: The REE + Y compositions of Zunyi samples; Table S3: Sr isotope compositions for Zunyi samples; Table S4: Nd isotope compositions for Zunyi samples.

Author Contributions: Conceptualization: D.P. and H.Y.; writing: H.Y.; review and editing: D.P., L.X. and K.S. All authors have read and agreed to the published version of the manuscript.

Funding: This research was funded by National Natural Science Foundation of China (No. 41972091 and 42202071).

Data Availability Statement: Not applicable.

Acknowledgments: Thanks are given to Peng Yuan and Xuerui Fu for their assistance with the fieldwork.

Conflicts of Interest: The authors declare no conflict of interest.

References

1. Ali, J.R.; Thompson, G.M.; Zhou, M.F.; Song, X. Emeishan large igneous province, SW China. *Lithos* **2005**, *79*, 475–489. [\[CrossRef\]](#)
2. Huang, H.; Du, Y.S.; Yang, J.H.; Zhou, L.; Hu, L.S.; Huang, H.W.; Huang, Z.Q. Origin of Permian basalts and clastic rocks in Napo, Southwest China: Implications for the erosion and eruption of the Emeishan large igneous province. *Lithos* **2014**, *208–209*, 324–338. [\[CrossRef\]](#)
3. Shellnutt, J.G. The Emeishan large igneous province: A synthesis. *Geosci. Front.* **2014**, *5*, 369–394. [\[CrossRef\]](#)
4. Xu, Y.G.; Chung, S.L.; Shao, H.; He, B. Silicic magmas from the Emeishan large igneous province, Southwest China: Petrogenesis and their link with the endGuadalupian biological crisis. *Lithos* **2010**, *119*, 47–60. [\[CrossRef\]](#)
5. Zhou, M.F.; Zhao, J.H.; Qi, L.; Su, W.; Hu, R. Zircon U-Pb geochronology and elemental and Sr-Nd isotope geochemistry of Permian mafic rocks in the Funing area, SW China. *Contrib. Mineral. Petrol.* **2006**, *151*, 1–19. [\[CrossRef\]](#)
6. Zhu, B.; Guo, Z.J.; Zhang, S.N.; Ukstins, I.; Du, W.; Liu, R.C. What triggered the early-stage eruption of the Emeishan large igneous province? *Geol. Soc. Am. Bull.* **2019**, *131*, 1837–1856. [\[CrossRef\]](#)
7. Bond, D.P.G.; Hilton, J.; Wignall, P.B.; Ali, J.R.; Stevens, L.G.; Sun, Y.D.; Lai, X.L. The Middle Permian (Capitanian) mass extinction on land and in the oceans. *Earth Sci. Rev.* **2010**, *109*, 100–116. [\[CrossRef\]](#)
8. Yang, J.H.; Cawood, P.A.; Du, Y.S. Voluminous silicic eruptions during late Permian Emeishan igneous province and link to climate cooling. *Earth Planet. Sci. Lett.* **2015**, *432*, 166–175. [\[CrossRef\]](#)
9. Zhao, L.X.; Dai, S.F.; Graham, I.T.; Li, X.; Zhang, B.B. New insights into the lowest Xuanwei Formation in eastern Yunnan Province, SW China: Implications for Emeishan large igneous province felsic tuff deposition and the cause of the endGuadalupian mass extinction. *Lithos* **2016**, *264*, 375–391. [\[CrossRef\]](#)
10. Lai, X.L.; Wang, W.; Wignall, P.B.; Bond, D.; Jiang, H.S.; Ali, J.R.; John, E.H.; Sun, Y.D. Palaeoenvironmental change during the end-Guadalupian (Permian) mass extinction in Sichuan, China. *Palaeogeogr. Palaeoclimatol. Palaeoecol.* **2008**, *269*, 78–93. [\[CrossRef\]](#)
11. Wignall, P.B.; Sun, Y.D.; Bond, D.P.G.; Izon, G.; Newton, R.J.; Védérine, S.; Widdowson, M.; Ali, J.R.; Lai, X.L.; Jiang, H.S.; et al. Volcanism, mass extinction, and carbon isotope fluctuations in the Middle Permian of China. *Science* **2009**, *324*, 1179–1182. [\[CrossRef\]](#)
12. Ogg, J.G.; Ogg, G.; Gradstein, F.M. *The Concise Geologic Time Scale*; Elsevier: Amsterdam, The Netherlands, 2016; pp. 123–124.

13. Yan, H.; Pi, D.H.; Jiang, S.Y.; Hao, W.D.; Mänd, K.; Robbins, L.J.; Li, L.; Konhauser, K.O. New constraints on the onset age of the Emeishan LIP volcanism and implications for the Guadalupian mass extinction. *Lithos* **2020**, *360–361*, 105441. [[CrossRef](#)]
14. Jerram, D.A.; Widdowson, M.; Wignall, P.B.; Sun, Y.D.; Lai, X.L.; Bond, D.P.; Torsvik, T.H. Submarine palaeoenvironments during Emeishan flood basalt volcanism, SW China: Implications for plume-lithosphere interaction during the Capitanian, Middle Permian ('end Guadalupian') extinction event. *Palaeogeogr. Palaeoclimatol. Palaeoecol.* **2016**, *441*, 65–73. [[CrossRef](#)]
15. Wignall, P.B.; Védrine, S.; Bond, D.; Wang, W.; Lai, X.L.; Ali, J.R.; Jiang, H.S. Facies analysis and sea-level change at the Guadalupian–Lopingian Global Stratotype (Laibin, South China), and its bearing on the end-Guadalupian mass extinction. *J. Geol. Soc. Lond.* **2009**, *166*, 655–666. [[CrossRef](#)]
16. Bagherpour, B.; Bucher, H.; Schneebeili-Hermann, E.; Vennemann, T.; Chiaradia, M.; Shen, S.Z. Early late Permian coupled carbon and strontium isotope chemostratigraphy from South China: Extended Emeishan volcanism? *Gondwana Res.* **2018**, *58*, 58–70. [[CrossRef](#)]
17. Huang, H.; Hou, M.C.; Qing, H.R.; Zhou, L.; Yang, J.H.; Du, Y.S.; Tian, J.C.; Ni, S.J.; Xiong, F.H. The contribution of the Emeishan large igneous province to the strontium isotope evolution of the Capitanian seawater. *Int. Geol. Rev.* **2019**, *61*, 1927–1939. [[CrossRef](#)]
18. Bau, M. Effects of syn- and post-depositional processes on the rare-earth element distribution in Precambrian iron-formations. *Eur. J. Mineral.* **1993**, *5*, 257–267. [[CrossRef](#)]
19. Bau, M.; Dulski, P. Distribution of yttrium and rare-earth elements in the Penge and Kuruman iron-formations, Transvaal supergroup, South Africa. *Precambrian Res.* **1996**, *79*, 37–55. [[CrossRef](#)]
20. Bau, M.; Schmidt, K.; Koschinsky, A.; Hein, J.; Kuhn, T.; Usui, A. Discriminating between different genetic types of marine ferro-manganese crusts and nodules based on rare earth elements and yttrium. *Chem. Geol.* **2014**, *381*, 1–9. [[CrossRef](#)]
21. Stille, P.; Clauer, N.; Abrecht, J. Nd isotopic composition of Jurassic Tethys seawater and the genesis of Alpine Mn-deposits: Evidence from Sr–Nd isotope data. *Geochim. Cosmochim. Acta* **1989**, *53*, 1095–1099. [[CrossRef](#)]
22. Konhauser, K.O.; Planavsky, N.J.; Hardisty, D.S.; Robbins, L.J.; Warchola, T.J.; Haugaard, R.; Lalonde, S.V.; Partin, C.A.; Oonk, P.B.H.; Tsikos, H.; et al. Iron formations: A global record of Neoproterozoic to Palaeoproterozoic environmental history. *Earth Sci. Rev.* **2017**, *172*, 140–177. [[CrossRef](#)]
23. Bau, M.; Moller, P.; Dulski, P. Yttrium and lanthanides in eastern Mediterranean seawater and their fractionation during redox-cycling. *Mar. Chem.* **1997**, *56*, 123–131. [[CrossRef](#)]
24. Bau, M.; Hohendorf, A.; Dulski, P.; Beukes, N.J. Sources of rare-earth elements and iron in paleoproterozoic iron-formations from the Transvaal supergroup, South Africa: Evidence from neodymium isotopes. *J. Geol.* **1997**, *105*, 121–129. [[CrossRef](#)]
25. Kamber, B.S.; Webb, G.E. The geochemistry of late Archean microbial carbonate: Implications for ocean chemistry and continental erosion history. *Geochim. Cosmochim. Acta* **2001**, *65*, 2509–2525. [[CrossRef](#)]
26. Alexander, B.; Bau, M.; Andersson, P.; Dulski, P. Continentally-derived solutes in shallow Archean seawater: Rare earth element and Nd isotope evidence in iron formation from the 2.9 Ga Pongola supergroup. *Geochim. Cosmochim. Acta* **2008**, *72*, 378–394. [[CrossRef](#)]
27. Alexander, B.; Bau, M.; Andersson, P. Neodymium isotopes in Archean seawater and implications for the marine Nd cycle in Earth's early oceans. *Earth Planet. Sci. Lett.* **2009**, *283*, 144–155. [[CrossRef](#)]
28. Viehmann, S.; Hoffmann, J.E.; Münker, C.; Bau, M. Decoupled Hf–Nd isotopes in Neoproterozoic seawater reveal weathering of emerged continents. *Geology* **2014**, *42*, 115–118. [[CrossRef](#)]
29. Blaser, P.; Lippold, J.; Gutjahr, M.; Frank, N.; Link, J.M.; Frank, M. Extracting foraminiferal seawater Nd isotope signatures from bulk deep sea sediment by chemical leaching. *Chem. Geol.* **2016**, *439*, 189–204. [[CrossRef](#)]
30. Gao, J.B.; Yang, R.D.; Xu, H.; Zhang, X.; Feng, K.N.; Zheng, L.L. Genesis of Permian sedimentary manganese deposits in Zunyi, Guizhou Province, SW China: Constraints from geology and elemental geochemistry. *J. Geochem. Explor.* **2018**, *192*, 142–154. [[CrossRef](#)]
31. Xu, H.; Gao, J.B.; Yang, R.D.; Feng, K.N.; Wang, L.B.; Chen, J. Metallogenic mechanism of large manganese deposits from Permian manganese ore belt in western South China Block: New mineralogical and geochemical evidence. *Ore Geol. Rev.* **2021**, *132*, 103993. [[CrossRef](#)]
32. Yan, H.; Pi, D.H.; Jiang, S.Y.; Mao, J.W.; Xu, L.G.; Yang, X.Q.; Hao, W.D.; Mänd, K.; Li, L.; Konhauser, K.O.; et al. Mineral paragenesis in Paleozoic manganese ore deposits: Depositional versus post-depositional formation processes. *Geochim. Cosmochim. Acta* **2022**, *325*, 65–86. [[CrossRef](#)]
33. Yu, W.C.; Polgari, M.; Du, Y.S. Microbial metallogenesis of Cryogenian manganese ore deposits in South China. *Precambrian Res.* **2019**, *322*, 122–135. [[CrossRef](#)]
34. Domeier, M.; Torsvik, T.H. 2014, Plate tectonics in the late Paleozoic. *Geosci. Front.* **2014**, *5*, 303–350. [[CrossRef](#)]
35. Editing Committee of Stratigraphy (ECS). *Permian in China*; Geological Publishing House: Beijing, China, 2000; p. 149. (In Chinese with English abstract)
36. He, B.; Xu, Y.G.; Huang, X.L.; Luo, Z.Y.; Shi, Y.R.; Yang, Q.J.; Yu, S.Y. Age and duration of the Emeishan flood volcanism, SW China: Geochemistry and SHRIMP zircon U–Pb dating of silicic ignimbrites, post-volcanic Xuanwei Formation and clay tuff at the Chaotian section. *Earth Planet. Sci. Lett.* **2007**, *255*, 306–323. [[CrossRef](#)]

37. Sun, Y.D.; Lai, X.L.; Wignall, P.B.; Widdowson, M.; Ali, J.R.; Jiang, H.S.; Wang, W.; Yan, C.B.; Bond, D.P.; Védérine, S. Dating the onset and nature of the middle Permian Emeishan large igneous province eruptions in SW China using conodont biostratigraphy and its bearing on mantle plume uplift models. *Lithos* **2010**, *119*, 20–33. [[CrossRef](#)]
38. He, B.; Xu, Y.G.; Chung, S.L.; Xiao, L.; Wang, Y. Sedimentary evidence for a rapid, kilometer-scale crustal doming prior to the eruption of the Emeishan flood basalts. *Earth Planet. Sci. Lett.* **2003**, *213*, 391–405. [[CrossRef](#)]
39. Saitoh, M.; Isozaki, Y.; Yao, J.X.; Ji, Z.S.; Ueno, Y.; Yoshida, N. The appearance of an oxygen-depleted condition on the Capitanian disphotic slope/basin in South China: Middle-Upper Permian stratigraphy at Chaotian in northern Sichuan. *Glob. Planet. Change* **2013**, *105*, 180–192. [[CrossRef](#)]
40. Pu, W.; Gao, J.F.; Zhao, K.D.; Ling, H.F.; Jiang, S.Y. Separation method of Rb-Sr, Sm-Nd using DCTA and HIBA. *J. Nanjing University (Nat. Sci.)* **2005**, *41*, 445–450. (In Chinese with English abstract)
41. Tanaka, T.; Togashi, S.; Kamioka, H.; Amakawa, H.; Kagami, H.; Hamamoto, T.; Yuhara, M.; Orihashi, Y.; Yoneda, S.; Shimizu, H.; et al. JNdi-1: A neodymium isotopic reference in consistency with LaJolla neodymium. *Chem. Geol.* **2000**, *168*, 279–281. [[CrossRef](#)]
42. Bau, M.; Dulski, P. Comparing yttrium and rare earths in hydrothermal fluids from the Mid-Atlantic Ridge: Implications for Y and REE behaviour during near-vent mixing and for the Y/Ho ratio of Proterozoic seawater. *Chem. Geol.* **1999**, *155*, 77–90. [[CrossRef](#)]
43. Douville, E.; Bienvénu, P.; Charlou, J.L.; Donval, J.P.; Fouquet, Y.; Appriou, P.; Gamo, T. Yttrium and rare earth elements in fluids from various deep-sea hydrothermal systems. *Geochim. Cosmochim. Acta* **1999**, *63*, 627–643. [[CrossRef](#)]
44. Ma, C.Q.; Ehlers, C.; Xu, C.H.; Li, Z.C.; Yang, K.G. The roots of the Dabieshan ultrahigh-pressure metamorphic terrain: Constraints from geochemistry and Nd–Sr isotope systematics. *Precambrian Res.* **2000**, *102*, 279–301. [[CrossRef](#)]
45. Wang, C.Y.; Zhou, M.F.; Qi, L. Permian flood basalts and mafic intrusions in the Jinping (SW China)–Song Da (northern Vietnam) district: Mantle sources, crustal contamination and sulfide segregation. *Chem. Geol.* **2007**, *243*, 317–343. [[CrossRef](#)]
46. Morford, J.L.; Emerson, S. The geochemistry of redox sensitive trace metals in sediments. *Geochim Cosmochim. Acta.* **1999**, *63*, 1735–1750. [[CrossRef](#)]
47. Bau, M. Scavenging of dissolved yttrium and rare earths by precipitating iron oxyhydroxide: Experimental evidence for Ce oxidation, Y–Ho fractionation, and lanthanide tetrad effect. *Geochim. Cosmochim. Acta* **1999**, *63*, 67–77. [[CrossRef](#)]
48. Pi, D.H.; Liu, C.Q.; Shields-Zhou, G.A.; Jiang, S.Y. Trace and rare earth element geochemistry of black shale and kerogen in the early Cambrian Niutitang Formation in Guizhou province, South China: Constraints for redox environments and origin of metal enrichments. *Precamb. Res.* **2013**, *225*, 218–229. [[CrossRef](#)]
49. Shields, G.; Stille, P. Diagenetic constraints on the use of cerium anomalies as palaeoseawater redox proxies: An isotopic and REE study of Cambrian phosphorites. *Chem. Geol.* **2001**, *175*, 29–48. [[CrossRef](#)]
50. Zhu, B.; Jang, S.Y.; Yang, J.H.; Pi, D.H.; Ling, H.F.; Chen, Y.Q. Rare earth element and Sr-Nd isotope geochemistry of phosphate nodules from the lower Cambrian Niutitang Formation, NW Hunan Province, South China. *Palaeogeogr. Palaeoclimatol. Palaeoecol.* **2014**, *398*, 132–143. [[CrossRef](#)]
51. Xin, H.; Jang, S.H.; Yang, J.H.; Wu, H.P.; Pi, D.H. Rare earth element and Sr-Nd isotope geochemistry of phosphatic rocks in Neoproterozoic Ediacaran Doushantuo Formation in Zhangcunping section from western Hubei Province, South China. *Palaeogeogr. Palaeoclimatol. Palaeoecol.* **2015**, *440*, 712–724. [[CrossRef](#)]
52. Wright, J.; Schrader, H.; Holser, W.T. Paleoredox variations in ancient oceans recorded by rare earth elements in fossil apatite. *Geochim. Cosmochim. Acta* **1987**, *51*, 631–644. [[CrossRef](#)]
53. Pourret, O.; Davranche, M.; Gruau, G.; Dia, A. New insights into cerium anomalies in organic-rich alkaline waters. *Chem. Geol.* **2008**, *251*, 120–127. [[CrossRef](#)]
54. Xiong, Z.; Li, T.; Algeo, T.; Chang, F.; Yin, X.; Xu, Z. Rare earth element geochemistry of laminated diatom mats from tropical West Pacific: Evidence for more reducing bottomwaters and higher primary productivity during the Last Glacial Maximum. *Chem. Geol.* **2012**, *296*, 103–118. [[CrossRef](#)]
55. Byrne, R.H.; Kim, K.-H. Rare earth element scavenging in seawater. *Geochim. Cosmochim. Acta* **1990**, *54*, 2645–2656. [[CrossRef](#)]
56. Ohta, A.; Kawabe, I. REE(III) adsorption onto Mn dioxide (δ -MnO₂) and Fe oxyhydroxide: Ce(III) oxidation by δ -MnO₂. *Geochim. Cosmochim. Acta* **2001**, *65*, 695–703. [[CrossRef](#)]
57. Davranche, M.; Pourret, O.; Gruau, G.; Dia, A.; Jin, D.; Gaertner, D. Competitive binding of REE to humic acid and manganese oxide: Impact of reaction kinetics on development of cerium anomaly and REE adsorption. *Chem. Geol.* **2008**, *247*, 154–170. [[CrossRef](#)]
58. Pourret, O.; Davranche, M. Rare earth element sorption onto hydrous manganese oxide: A modeling study. *J. Colloid Interface Sci.* **2013**, *395*, 18–23. [[CrossRef](#)]
59. Bau, M.; Koschinsky, A. Oxidative scavenging of cerium on hydrous Fe oxide: Evidence from the distribution of rare earth elements and yttrium between Fe oxides and Mn oxides in hydrogenetic ferromanganese crusts. *Geochem. J.* **2009**, *43*, 37–47. [[CrossRef](#)]
60. Bau, M.; Koschinsky, A.; Dulski, P.; Hein, J.R. Comparison of the partitioning behaviours of yttrium, rare earth elements, and titanium between hydrogenetic marine ferromanganese crusts and seawater. *Geochim. Cosmochim. Acta* **1996**, *60*, 1709–1725. [[CrossRef](#)]

61. Holser, W.T. Evaluation of the application of rare-earth elements to paleoceanography. *Palaeogeogr. Palaeoclimatol. Palaeoecol.* **1997**, *132*, 309–323. [[CrossRef](#)]
62. Mills, R.A.; Wells, D.M.; Roberts, S. Genesis of ferromanganese crusts from the TAG hydrothermal field. *Chem. Geol.* **2001**, *176*, 283–293. [[CrossRef](#)]
63. Murphy, E.; McMurtry, G.M.; Kim, K.H.; De Carlo, E.H. Geochemistry and geochronology of a hydrothermal ferromanganese deposit from the North Fiji Basin. *Mar. Geol.* **1991**, *98*, 297–312. [[CrossRef](#)]
64. Surya Prakash, L.; Ray, D.; Paropkari, A.L.; Mudholkar, A.V.; Satyanarayanan, M.; Sreenivas, B.; Chandrasekharam, D.; Kota, D.; Kamesh Raju, K.A.; Kaisary, S.; et al. Distribution of REEs and yttrium among major geochemical phases of marine Fe–Mn-oxides: Comparative study between hydrogenous and hydrothermal deposits. *Chem. Geol.* **2012**, *312–313*, 127–137. [[CrossRef](#)]
65. Beukes, N.J.; Swindell, E.P.W.; Wabo, H. Manganese deposits of Africa. *Episodes* **2016**, *39*, 285–317. [[CrossRef](#)]
66. Viehmann, S.; Bau, M.; Smith, A.J.B.; Beukes, N.J.; Dantas, E.L.; Bühn, B. The reliability of ~2.9 Ga old Witwatersrand banded iron formations (South Africa) as archives for Mesoarchean seawater: Evidence from REE and Nd isotope systematics. *J. Afr. Earth Sci.* **2015**, *111*, 322–334. [[CrossRef](#)]
67. Palmer, M.R.; Edmond, J.M. The strontium isotope budget of the modern ocean. *Earth Planet. Sci. Lett.* **1989**, *92*, 11–26. [[CrossRef](#)]
68. Taylor, A.S.; Lasaga, A.C. The role of basalt weathering in the Sr isotope budget of the oceans. *Chem. Geol.* **1999**, *161*, 199–214. [[CrossRef](#)]
69. Elderfield, H. Strontium isotope stratigraphy. *Palaeogeogr. Palaeoclimatol. Palaeoecol.* **1986**, *57*, 71–90. [[CrossRef](#)]
70. Pearce, C.R.; Parkinson, I.J.; Gaillardet, J.; Charlier, B.L.A.; Mokadem, F.; Burton, K.W. Reassessing the stable (d88/86Sr) and radiogenic(87Sr/86Sr) strontium isotopic composition of marine inputs. *Geochim. Cosmochim. Acta* **2015**, *157*, 125–146. [[CrossRef](#)]
71. Brand, U.; Logan, A.; Hiller, N.; Richardson, J. Geochemistry of modern brachiopods: Applications and implications for oceanography and paleoceanography. *Chem. Geol.* **2003**, *198*, 305–334. [[CrossRef](#)]
72. Kani, T.; Fukui, M.; Isozaki, Y.; Nohda, S. The Paleozoic minimum of 87Sr/86Sr ratio in the Capitanian (Permian) mid-oceanic carbonates: A critical turning point in the Late Paleozoic. *J. Asian Earth Sci.* **2008**, *32*, 22–33. [[CrossRef](#)]
73. Kani, T.; Hisanabe, C.; Isozaki, Y. The Capitanian (Permian) minimum of 87Sr/86Sr ratio in the mid-Panthalassan paleo-atoll carbonates and its demise by deglaciation and continental doming. *Gondwana Res.* **2013**, *24*, 212–221. [[CrossRef](#)]
74. Korte, C.; Jasper, T.; Kozur, H.W.; Veizer, J. 87Sr/86Sr record of Permian seawater. *Palaeogeogr. Palaeoclimatol. Palaeoecol.* **2006**, *240*, 89–107. [[CrossRef](#)]
75. Bau, M.; Dulski, P. Comparative study of yttrium and rare-earth element behaviours in fluorine-rich hydrothermal fluids. *Contrib. Miner. Petrol.* **1995**, *119*, 213–223. [[CrossRef](#)]
76. Klein, C.; Beukes, N.J. Geochemistry and sedimentology of a facies transition from limestone to iron-formation deposition in the early Proterozoic Transvaal Supergroup, South Africa. *Econ. Geol.* **1989**, *84*, 1733–1774. [[CrossRef](#)]
77. Goldstein, S.L.; Hemming, S.R. Long-lived isotopic tracers in oceanography, paleoceanography, and ice-sheet dynamics. In *Treatise on Geochemistry*; Elsevier: Amsterdam, The Netherlands, 2003; pp. 453–489.
78. Frank, M. Radiogenic isotopes: Tracers of past ocean circulation and erosional input. *Rev. Geophys.* **2002**, *40*, 1. [[CrossRef](#)]
79. Piepgras, D.J.; Wasserburg, G.J. Neodymium isotopic variations in seawater. *Earth Planet. Sci. Lett.* **1980**, *50*, 128–138. [[CrossRef](#)]
80. German, C.R.; Von Damm, K.L. Hydrothermal processes. In *Treatise on Geochemistry*; Turekian, K.K., Holland, H.D., Eds.; Elsevier: Oxford, UK, 2014; Volume 8, pp. 191–233.
81. Halliday, A.N.; Davidson, J.P.; Holden, P.; Owen, R.M.; Olivarez, A.M. Metalliferous sediments and the scavenging residence time of Nd near hydrothermal vents. *Geophys. Res. Lett.* **1992**, *19*, 761–764. [[CrossRef](#)]
82. Jeandel, C. Concentration and isotopic composition of Nd in the South Atlantic Ocean. *Earth Planet. Sci. Lett.* **1993**, *117*, 581–591. [[CrossRef](#)]
83. Tachikawa, K.; Jeandel, C.; Roy-Barman, M. A new approach to the Nd residence time in the ocean: The role of atmospheric inputs. *Earth Planet. Sci. Lett.* **1999**, *170*, 433–446. [[CrossRef](#)]
84. Keto, L.S.; Jacobsen, S.B. Nd isotopic variations of Phanerozoic paleoceans. *Earth Planet. Sci. Lett.* **1988**, *90*, 395–410. [[CrossRef](#)]
85. Ali, J.R.; Fitton, J.G.; Herzberg, C. Emeishan large igneous province (SW China) and the mantle-plume up-doming hypothesis. *J. Geol. Soc.* **2010**, *167*, 953–959. [[CrossRef](#)]

Disclaimer/Publisher’s Note: The statements, opinions and data contained in all publications are solely those of the individual author(s) and contributor(s) and not of MDPI and/or the editor(s). MDPI and/or the editor(s) disclaim responsibility for any injury to people or property resulting from any ideas, methods, instructions or products referred to in the content.